PNAS RESEARCH ARTICLE | MICROBIOLOGY

Identification of a depupylation regulator for an essential enzyme in *Mycobacterium tuberculosis*

Shoshanna C. Kahne[a], Jin Hee Yoo[a], James Chen[b], Kehilwe Nakedi[c], Lakshminarayan M. Iyer[d], Gregory Putzel[a,e,f], Nora M. Samhadaneh[a,e,f], Alejandro Pironti[a,e,f], L. Aravind[d], Damian C. Ekiert[a,b,g], Gira Bhabha[b,g], Kyu Y. Rhee[c], and K. Heran Darwin[a,1]

Affiliations are included on p. 10.

Edited by Kim Orth, Department of Molecular Biology, The University of Texas Southwestern Medical Center, Dallas, TX; received April 10, 2024; accepted October 8, 2024

In *Mycobacterium tuberculosis (Mtb)*, proteins that are posttranslationally modified with a prokaryotic ubiquitin-like protein (Pup) can be degraded by bacterial proteasomes. A single Pup-ligase and depupylase shape the pupylome, but the mechanisms regulating their substrate specificity are incompletely understood. Here, we identified a depupylation regulator, a protein called CoaX, through its copurification with the depupylase Dop. CoaX is a pseudopantothenate kinase that showed evidence of binding to pantothenate, an essential nutrient *Mtb* synthesizes, but not its phosphorylation. In a Δ*coaX* mutant, pantothenate synthesis enzymes including PanB, a substrate of the Pup-proteasome system (PPS), were more abundant than in the parental strain. In vitro, CoaX specifically accelerated depupylation of Pup~PanB, while addition of pantothenate inhibited this reaction. In culture, media supplementation with pantothenate decreased PanB levels, which required CoaX. Collectively, we propose CoaX regulates PanB abundance in response to pantothenate levels by modulating its vulnerability to proteolysis by *Mtb* proteasomes.

Mycobacterium | pantothenate | proteasome | Pup | depupylation

Mycobacterium tuberculosis (*Mtb*), the causative agent of tuberculosis (TB), is responsible for an ancient and enduring global pandemic. While about 85% of TB cases are curable, therapies are burdensome, typically requiring 4 to 6 mo of antibiotic treatment for drug-susceptible strains (1). Barriers of access to treatment, among other factors, contributed to an estimated 1.6 million deaths from TB in 2021 (1). Increased mechanistic understanding of *Mtb* biology may reveal new approaches for tackling this devastating pandemic.

The Pup-proteasome system (PPS), an ATP-dependent proteolytic pathway in *Mtb*, contributes to virulence in mouse infection models (2–6). Like the eukaryotic protein ubiquitin, prokaryotic ubiquitin-like protein (Pup) can be posttranslationally attached to surface exposed lysines, targeting proteins for degradation by proteasomes. Like ubiquitylation, pupylation is reversible (7–9). In contrast to eukaryotes that attach ubiquitin in a multistep process and encode hundreds of ligases and dozens of deubiquitylases that confer specificity, only two enzymes are required for the pupylation and depupylation of dozens of proteins in mycobacteria.

In *Mtb*, Pup is translated with a carboxyl (C)-terminal glutamine that must be deamidated by the enzyme deamidase of Pup (Dop), converting it to glutamate, before Pup can be ligated to other proteins by proteasome accessory factor A (PafA) (10, 11). Dop can also reverse this pupylation reaction and is necessary to maintain Pup levels in the cell (4, 12, 13). Pup-dependent degradation by proteasomes requires pupylated proteins to be recruited by a homohexameric complex of mycobacterial proteasome ATPase (Mpa; also called AAA ATPase forming ring-shaped complexes, or ARC, in nonmycobacteria species) (8, 14, 15). In the absence of Mpa, the 28-subunit bacterial proteasome is gated and cannot degrade pupylated proteins (16, 17). Complexing between the C termini of the Mpa hexamer and the proteasome leads to opening of the proteolytic compartment, and ATP hydrolysis by Mpa powers pupylated protein unfolding and entry (18–20). While the enzymatic mechanisms of PafA, Dop, Mpa, and the proteasome have been extensively characterized, little is known about how their activities are regulated [reviewed in (21)].

The steady-state abundance of a protein that can be pupylated is a function of PafA and Dop activity, as well as how it is delivered to a proteasome core protease. Global changes in pupylated proteins, the "pupylome," in response to growth conditions have been described in both *Mtb* (22) and *Mycobacterium smegmatis* (*Msm*) (23), but the molecular mechanisms underlying these phenotypes are unknown. Furthermore,

Significance

For centuries, *Mycobacterium tuberculosis*, the causative agent of tuberculosis, has remained one of the greatest killers of humankind by a single infectious organism. Mycobacteria use proteasomes to degrade proteins posttranslationally tagged with a protein called prokaryotic ubiquitin-like protein (Pup). While enzymes that catalyze pupylation and depupylation have been identified, little is known about how their activities can be regulated to target specific substrates. Here, we report the identification of a protein, CoaX, and a metabolite, pantothenate, that regulate depupylation of an essential enzyme in pantothenate synthesis. Our data provide a mechanism of regulation of the Pup-proteasome system (PPS) that responds to cellular metabolic needs, giving critical insight into how the stability of other proteasome substrates might be regulated.

Preprint server: https://doi.org/10.1101/2024.03.29.587195.

The authors declare no competing interest.

This article is a PNAS Direct Submission.

[1]To whom correspondence may be addressed. Email: heran.darwin@nyulangone.org.

This article contains supporting information online at https://www.pnas.org/lookup/suppl/doi:10.1073/pnas.2407239121/-/DCSupplemental.

Published November 25, 2024.

motifs defining pupylation targets have been elusive. Verified PPS substrates are pupylated with variable efficiency in vitro and amino acid charges proximal to the targeted lysine in the three-dimensional conformation of substrates only partially explain this variation (24).

Depupylation efficiency also varies in vitro, and it has been hypothesized that differential steric hindrance associated with the positioning of Pup-modified substrates in the Dop active site confers this variability (25, 26). Steric hindrance may be affected by substrate interactions with the Dop loop, a conserved stretch of approximately 40 amino acids that is inferred to be disordered and proximal to the active site based on a crystal structure of Dop from *Acidothermus cellulolyticus* (27). Deletion of the Dop loop can accelerate depupylation in vitro (26) and yields diminished pupylomes in *Msm* and *Mtb* (26, 28). While these data reveal intrinsic factors affecting Dop activity, they do not explain how depupylation of a specific substrate could be differentially regulated in response to cellular needs or environmental conditions.

In this study, we found CoaX (Rv3600c) regulated depupylation of pupylated PanB (Pup~PanB). PanB is an essential enzyme that catalyzes an early committed step in pantothenate (vitamin B5) synthesis in mycobacteria. In the presence of excess pantothenate, the ultimate product of the PanB pathway, depupylation by Dop was inhibited in a CoaX-dependent manner, targeting more PanB for proteasomal degradation. Thus, we propose PanB levels in *Mtb* are regulated by a negative feedback loop mediated by CoaX, pantothenate, and the PPS.

Results

CoaX, A Predicted Pantothenate Kinase, Copurifies with Dop from *Mtb*. To identify potential depupylation regulators, we immunoprecipitated C-terminally epitope-tagged Dop ("Dop_{TAP}") from *Mtb* lysates. As a control, we also immunoprecipitated tagged PafA ("$PafA_{TAP}$") from lysates (*SI Appendix*, Table S1 for plasmids and strains). We observed a 25 to 37 kD protein that copurified with Dop_{TAP} but not $PafA_{TAP}$ (Fig. 1*A*). Excision of this band and mass spectrometry (MS) identified this protein as CoaX (Rv3600c), a predicted type-III pantothenate kinase (PanK) (Dataset S1). MS of all proteins that immunoprecipitated with Dop and PafA revealed CoaX was the fourth-most abundant protein in Dop purifications and undetectable in the PafA purifications (Dataset S2). CoaX has never been identified as a member of the pupylome, and immunoblotting with a monoclonal antibody to Pup did not reveal pupylated CoaX in the Dop immunoprecipitations (Fig. 1*B*).

PanK enzymes phosphorylate pantothenate in the first step of coenzyme A (coASH) synthesis (29) and are categorized into three types. Type I PanK enzymes (herein referred to as CoaA) belong to the P-loop kinase family (30, 31), while type II and type III enzymes belong to the acetate and sugar kinases/Hsc70/actin superfamily (type III PanK enzymes herein referred to as CoaX) (32). Many bacteria, including *Mtb*, are predicted to encode more than one PanK enzyme; however, the biological consequences of encoding multiple PanK enzymes have been studied in few species. CoaA and CoaX from *Bacillus subtilis* are both active in vitro and either is individually sufficient to support life (33). In *Bacillus anthracis,* CoaX is active in vitro and essential for viability, while a gene encoding a protein with homology to type II PanK enzymes does not show activity in vitro (34, 35).

In *Mtb*, CoaA, but not CoaX, is essential and has kinase activity in vitro (36). *coaX* is found across mycobacteria, including in *Mycobacterium leprae* (*Mlp*), the causative agent of leprosy. Because of its reduced functional genome size compared to *Mtb* (37), genes conserved in *Mlp*, which include those encoding PPS and pantothenate synthesis enzymes, are thought to be part of a minimal core genome required for the survival of this obligate intracellular organism.

Dop Forms a Complex with a Trimer of CoaX Dimers. To structurally characterize the Dop and CoaX interaction, we coproduced CoaX, Dop_{Msm}, and amino (N)-terminally truncated Pup (Pup_{91}) in *Escherichia coli* (*E. coli*) with an N-terminal tag on Pup for affinity purification. We first attempted to isolate complexes using a hexahistidine (His_6) tag on Pup_{91} and no tags Dop_{Msm} or CoaX (*SI Appendix*, Table S1 for plasmids and strains); however, we were unable to isolate Pup-Dop-CoaX complexes with this tag. Replacement of the His_6 tag with a Twin-Strep tag allowed robust purification of complexes (Fig. 1*C*). We obtained a cryoelectron microscopy (cryo-EM) structure of a trimer of CoaX dimers bound to Dop_{Msm} and Pup_{91} (Fig. 1*D*) at 2.04 Å-resolution (*SI Appendix*, Figs. S1 and S2 and Table S2). We also obtained cryo-EM data of CoaX alone, which resulted in a trimer of CoaX dimers at 2.59 Å-resolution (*SI Appendix*, Figs. S3 *A–C* and S4 *A–F* and Table S2) and a dimer of CoaX dimers at 2.81 Å-resolution (*SI Appendix*, Fig. S3 *A*, *B*, and *D* and S4 *G–L* and *SI Appendix*, Table S2). Consistent with CoaX structures solved to date, the *Mtb* CoaX dimers in our structures were formed by the head-to-head interaction of two protomers (38–40). The trimer arrangement of CoaX dimers observed in our structures is similar to the CoaX assembly from *Thermotoga maritima* ($CoaX_{Tmar}$) (38) and is largely similar in the presence or absence of Dop_{Msm} (RMSD: 1.3 Å over 1,324 atoms). The N-terminal domain of Dop_{Msm} is pincered by two CoaX dimers in this trimer assembly, creating an interface (~930 A^2) (41) composed of several hydrophobic and polar interactions, including hydrogen bonds and a salt bridge (Fig. 1*E* and *SI Appendix*, Fig. S5). Pup_{91} bound to Dop_{Msm} in a structurally similar pose as seen in the *Acidothermus cellulolyticus* Dop-Pup crystal structures (42), with two well-resolved helices (helix1 and helix2) interacting with Dop. This interaction positions the C-terminal amino acid of Pup near the active site of Dop_{Msm}. Notably, the C-terminal domain of Dop_{Msm} was largely disordered in our structure.

CoaX Is a Pseudokinase with Similarity to Type III Pantothenate Kinases. In agreement with a previous study (36), we did not detect hydrolysis of ATP by CoaX in the presence of pantothenate, while CoaA showed robust ATPase activity (Fig. 1*F*). While CoaX amino acid sequences are conserved across diverse bacterial species, two amino acids [arginine (R) 8 and histidine (H) 229 in *Mtb* CoaX] are mostly restricted to PPS-encoding actinobacteria (*SI Appendix*, Fig. S6). To test whether these residues contribute to the lack of observed CoaX activity, we made a double mutant ($CoaX_{DM}$) in which both residues were changed to glycine, the most common amino acid found at these positions in non-PPS-containing species (*SI Appendix*, Fig. S6). We found that $CoaX_{DM}$ had measurable ATPase activity in vitro, albeit lower than that of CoaA (Fig. 1*F*). Recently, a similar approach was used to interrogate the lack of measurable activity of a human pantothenate kinase (HsPANK4). Like $CoaX_{DM}$, replacement of two residues to the amino acids conserved in functional PanKs partially restores activity (43). Based on these results, we concluded that, like HsPANK4, *Mtb* CoaX likely evolved from a functional PanK through the acquisition of at least two substitutions, diminishing its PanK activity.

Given the structural similarity of *Mtb* CoaX to CoaX-family kinases, we used differential scanning fluorimetry (DSF) to assess binding of pantothenate. *Mtb* CoaX thermostability was

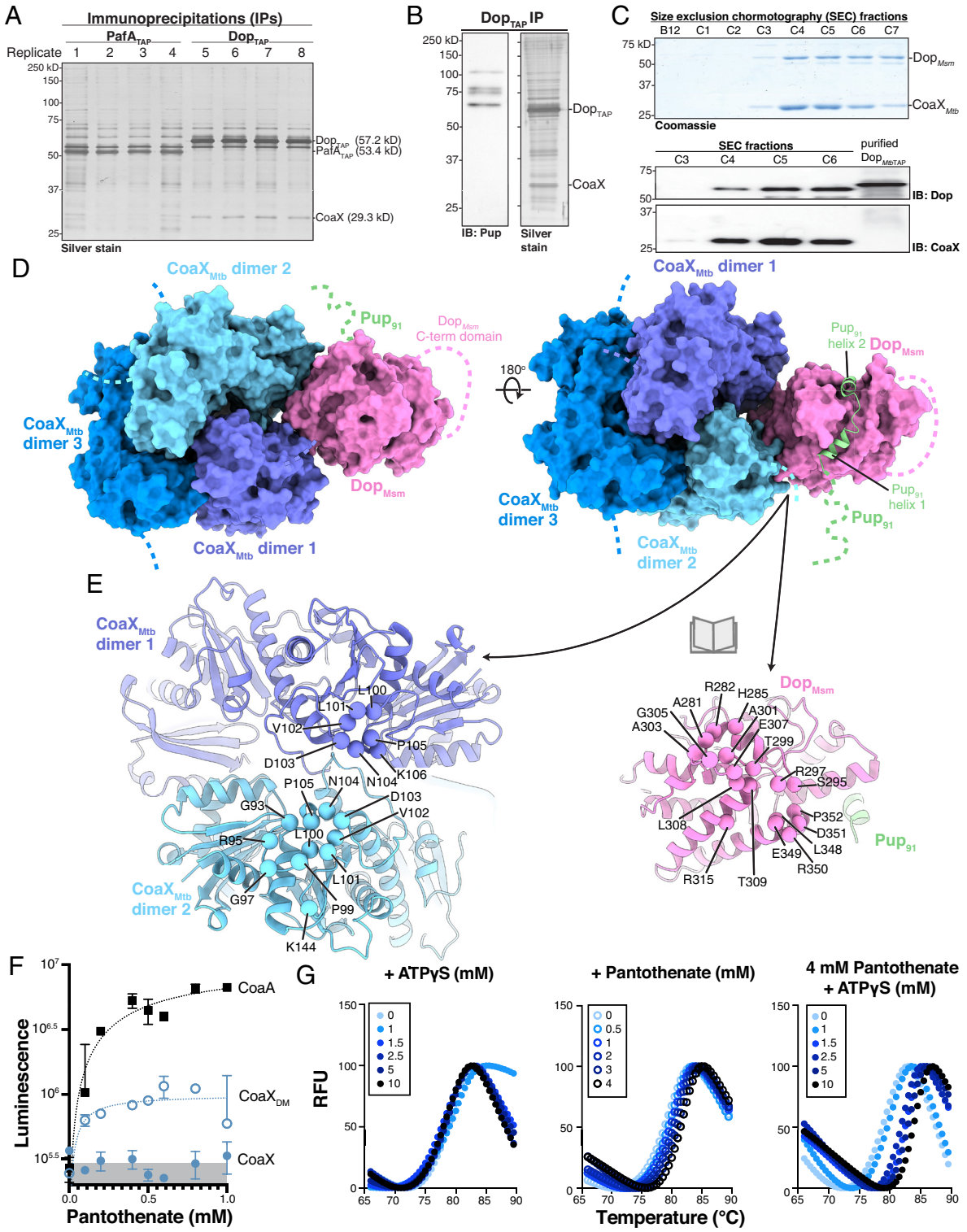

Fig. 1. Dop interacts with CoaX, a pseudopantothenate kinase. (*A*) Elutions from $PafA_{TAP}$ (lanes 1 to 4) and Dop_{TAP} (lanes 5 to 8) immunoprecipitations (IPs) from *Mtb* lysates were visualized by silver stain. Dop_{TAP}, $PafA_{TAP}$, and CoaX, a Dop-specific binding partner identified by mass spectrometry (Datasets S2 and S3), are indicated. (*B*) Elution from a Dop_{TAP} IP from *Mtb* lysate (*Left*) was analyzed with monoclonal antibodies to Pup. All proteins purified with Dop were visualized by silver stain (*Right*). Dop_{TAP} and CoaX are indicated. (*C*) CoaX and Dop_{Msm} coproduced and purified from *E. coli* lysate via interaction with $_{TwinStrep}Pup_{91}$ and Strep-Tactin XT resin were further purified by size exclusion chromatography (SEC) and fractions visualized by SDS-PAGE and Coomassie brilliant blue staining (*Top*) and immunoblotting against *Mtb* Dop or CoaX (*Bottom*). (*D*) Cryo-EM structure of CoaX, Dop_{Msm}, and Pup_{91}. Two views of the structure are shown with proteins rendered as cartoons superimposed on a transparent molecular surface. CoaX dimers are colored in shades of blue, Dop_{Msm} is colored pink, and Pup_{91} is colored green. Regions that are not modeled in the cryo-EM structure are indicated by dotted lines. (*E*) "Open book" representation of the right panel in (*D*), highlighting residues that make up the interface between CoaX (blue spheres) and Dop_{Msm} (magenta spheres). (*F*) CoaA (black squares), CoaX (blue circles), or $CoaX_{DM}$ (double mutant, CoaXR8G and H226G, blue open circles) activity was measured by ADP-Glo Luminescent assays (n = 2). Luminescence is proportional to ADP formation catalyzed by each enzyme in the presence of different concentrations of pantothenate. Empirically determined average baseline fluorescence of reactions containing no enzyme is indicated in gray. Michaelis–Menten curves for $CoaX_{DM}$ and CoaA are shown. (*G*) Differential scanning fluorimetry (DSF) to assess the thermal stability of CoaX with variable concentrations of ATPγS (*Left*), pantothenate (*Center*), or ATPγS in the presence of 4 mM pantothenate (*Right*).

unaffected by increasing concentrations of ATPγS alone (Fig. 1 *G*, *Left*). Increasing pantothenate concentration had a subtle effect on CoaX thermostability (Fig. 1*G*, *Center*), while increasing concentrations of ATPγS in the presence of pantothenate had the largest effect (Fig. 1 *G*, *Right*), suggesting CoaX bound both ATPγS and pantothenate. Together these results support the conclusion that *Mtb* CoaX is a pseudokinase that can bind but not phosphorylate pantothenate.

Deletion of *coaX* Leads to Increased Abundance of Pantothenate Synthesis Enzymes. We deleted most of the coding sequence of *coaX* from *Mtb* and replaced it with a hygromycin resistance cassette ("Δ*coaX*"), maintaining the start codon and 198 bp of sequence at the 3' end of the open reading frame to minimize potential polar effects on downstream genes (Fig. 2*A*). Loss of *coaX* had no effect on in vitro growth or on bacterial survival in the lungs or spleens of infected mice (*SI Appendix*, Fig. S7).

Given the association between CoaX and Dop, we hypothesized CoaX might affect the pupylated state of one or more substrates. To test this hypothesis, we visualized the pupylome of wild-type (WT), Δ*coaX*, and complemented strains by immunoblotting total cell lysates with monoclonal antibodies to Pup. We observed a unique pupylated species in the Δ*coaX* strain that was not present in the WT or complemented strains (Fig. 2*B*, arrowhead). Data-independent mass spectrometry (DIA-MS) revealed elevated levels of all enzymes involved in pantothenate synthesis (PanB, PanC, PanD, and PanG) and Rv2226, a protein of unknown function encoded downstream of PanB, in the Δ*coaX* mutant compared to the parental strain (Fig. 2*C*). Consistent with previous work supporting PanG as the exclusive ketopantoate reductase involved in pantothenate synthesis in *Mtb* (44), levels of IlvC and PanE, homologs of enzymes involved in pantothenate synthesis in other bacteria, did not change in the *coaX* mutant Dataset S3. PPS and coASH synthesis enzyme levels were equivalent in both strains (Fig. 2*C* and Dataset S3).

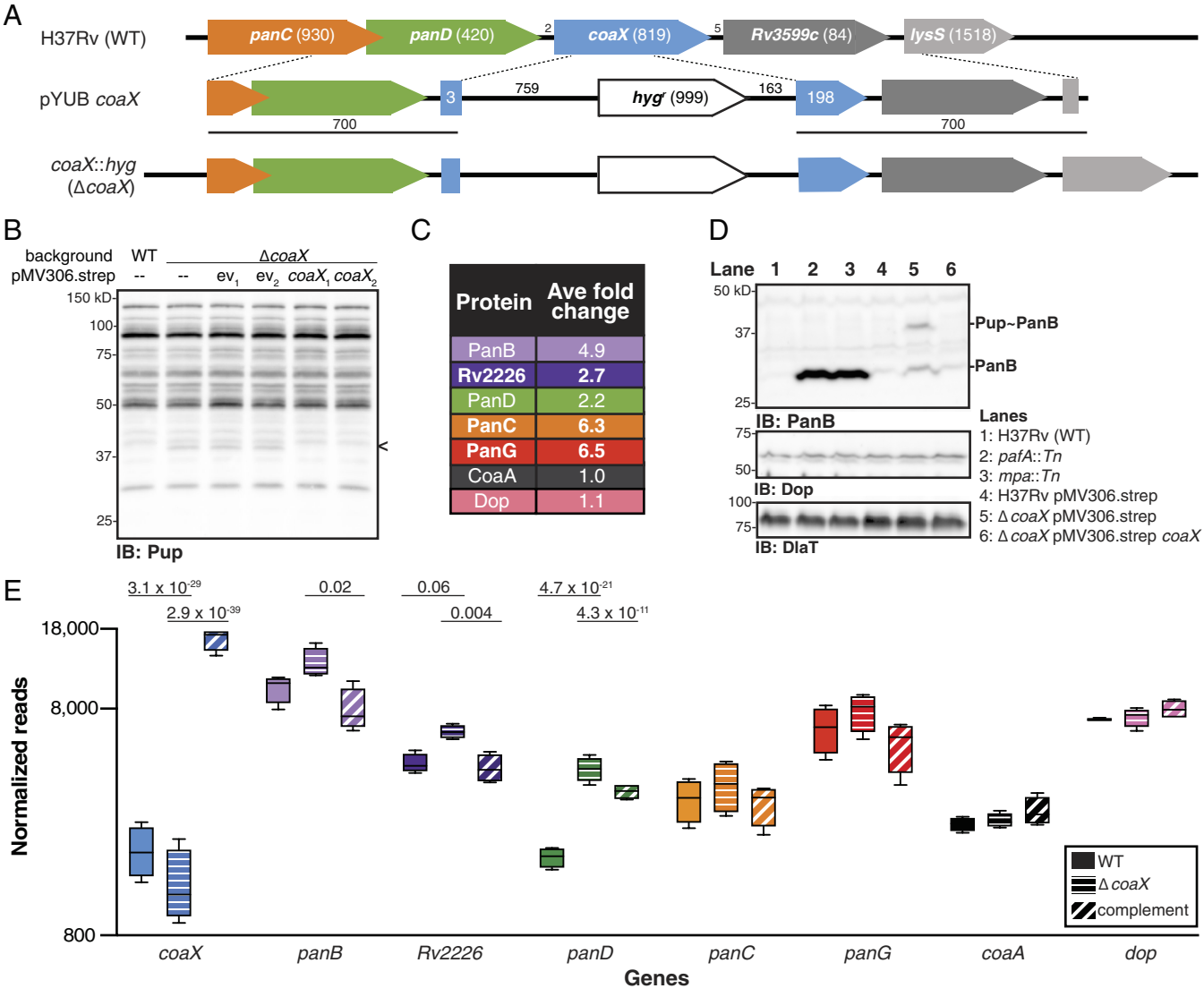

Fig. 2. Loss of *coaX* leads to accumulation of Pup~PanB. (*A*) *coaX* was deleted and replaced with a hygromycin selectable marker as described in the *Materials and Methods* (*SI Appendix*, Table S1 for plasmids and primers). Genes are not drawn to scale. Numbers in parentheses indicate gene length. "700" indicates length of flank sequences cloned into the allelic exchange vector. (*B*) Immunoblot against *Mtb* lysates using monoclonal antibodies to Pup. A unique pupylated protein in the *coaX* strains is indicated (<). (*C*) Average fold change of pantothenate synthesis-associated enzymes, CoaA, and Dop detected by DIA-MS in Δ*coaX* compared to WT strains. Proteins in bold were significantly more abundant in the mutant than in WT bacteria ($P < 0.05$). (*D*) Immunoblot of *Mtb* lysates using polyclonal antibodies to PanB, Dop, or DlaT (dihydrolipoamide acyltransferase, loading control). (*E*) Normalized reads associated with genes encoding pantothenate synthesis and PPS enzymes in RNA extracted from WT (solid bars), Δ*coaX* (horizontally black-striped bars), or a complemented strain (diagonally white-striped bars). Genes with differentially detected numbers of transcripts between different strains were deemed significant if the adjusted *P*-value was below a false discovery rate (Benjamini–Hochberg) of 0.1; such pairwise comparisons are indicated along with their adjusted *P*-values.

Among the proteins that were more abundant in the Δ*coaX* strain, PanB is the only known target of pupylation and proteasomal degradation (3, 8). Also, Pup~PanB migrates by SDS-PAGE to approximately 37 kD (8, 45), the same size as the pupylated species that specifically accumulated in the Δ*coaX* strain. To assess the abundance of endogenous PanB and Pup~PanB in various *Mtb* strains, we raised polyclonal rabbit antiserum to PanB for immunoblotting. Consistent with a previous experiment examining ectopically produced, epitope-tagged PanB (3), we observed low levels of endogenous PanB in WT *Mtb* and highly accumulated PanB in *pafA* and *mpa* mutants (Fig. 2*D*, lanes 1 to 3). As observed in the proteomics data, the Δ*coaX* strain contained more PanB than WT bacteria (Fig. 2*D*, compare lanes 1 and 5). Strikingly, in addition to PanB, a higher molecular weight species was observed in the Δ*coaX* strain and lost upon complementation with *coaX* in single copy (Fig. 2*D*, lane 5 compared to lanes 4 and 6). Because this larger, anti-PanB-reactive species specifically accumulated in the Δ*coaX* mutant and was the same size as the uniquely accumulated pupylated protein in this strain (Fig. 2*B*), we concluded this protein was Pup~PanB.

RNA-sequencing (RNA-Seq) revealed that loss of *coaX* led to increased transcripts associated with pantothenate synthesis enzymes and Rv2226 (Fig. 2*E*). We observed no changes in levels of transcripts associated with genes encoding PPS or coASH synthesis enzymes (Fig. 2*E* and Dataset S4). Together with the proteomics data, the RNA-seq supports the conclusion that loss of *coaX* results in a specific increase in pantothenate synthesis enzymes, in part, due to a change in transcript levels.

CoaX and Pantothenate Modulate Depupylation of Pup~PanB In Vitro. Given its physical association with Dop, we tested the effect of CoaX on depupylation of PanB and FabD, two model, pupylated proteasome substrates, in vitro. We purified tandemly tagged Pup~PanB or Pup~FabD from *Msm* and Dop_{Msm} from *E. coli*. PanB forms two, stacked, pentameric rings held together by interactions between the C termini of monomers in each ring (46). In vitro, PanB is pupylated at surface exposed lysines that extend from the top or bottom of a complex (45). Pup~PanB purified from *Msm* resulted in a mixture of pupylated and unpupylated species, which was apparent at the start of our in vitro reactions (*SI Appendix*, Fig. S8 *A* and *C*). FabD does not multimerize, thus, Pup~FabD was more homogenously purified from *Msm* leading to much less unpupylated substrate present at the start of the depupylation reactions (*SI Appendix*, Fig. S8 *B* and *D*).

As shown previously, Dop robustly depupylated Pup~PanB in vitro (Fig. 3*A*) (13, 25–27, 47). Addition of CoaX significantly accelerated depupylation of Pup~PanB but not Pup~FabD (Fig. 3*A* and *SI Appendix*, Fig. S8 *A* and *B*). Given that CoaX could bind pantothenate (Fig. 1*G*), we tested whether pantothenate affected CoaX-stimulated depupylation. Addition of pantothenate significantly inhibited CoaX-activated depupylation of Pup~PanB but not Pup~FabD (Fig. 3*B* and *SI Appendix*, Fig. S8 *C* and *D*). Pantothenate had no effect on reactions lacking CoaX or Dop_{Msm} (*SI Appendix*, Fig. S8*E*), thus pantothenate appears to specifically inhibit CoaX-activated depupylation of Pup~PanB.

CoaX and Pantothenate Regulate Depupylation of Pup~PanB in *Mtb*. We next tested whether pantothenate modulated PanB or Pup~PanB levels in bacteria. To do this, we exploited the fact that *Mtb* can use exogenous pantothenate (48), which is not a component of our standard culture media. We analyzed PanB levels in several strains by immunoblotting after growth in media containing different concentrations of pantothenate. Pantothenate supplementation reduced PanB levels in parental and complemented strains (Fig. 3*C*, lanes 1 to 3 and 7 to 9), but not in a Δ*coaX* strain (Fig. 3*C*, lanes 4 to 6).

Based on our in vitro data, we hypothesized that pantothenate supplementation would inhibit depupylation of Pup~PanB in WT bacteria, facilitating PanB turnover by the proteasome. To test this hypothesis, we repeated the pantothenate supplementation experiment with a mutant lacking the Pup-dependent proteasome activator, Mpa. Again, we observed low PanB levels in parental and complemented strains (Fig. 3*C*, lanes 10 to 12 and 16 to 18), but not in the *mpa* mutant (Fig. 3*C*, lanes 13 to 15). Pantothenate supplementation increased Pup~PanB levels in the *mpa* mutant (Fig. 3*C*, lanes 13 to 15). We observed no other changes in FabD, Dop, or pupylome levels in response to pantothenate supplementation in any strain (Fig. 3*C* and *SI Appendix*, Fig. S9). Finally, we treated the Δ*coaX* strain with the irreversible proteasome protease inhibitor epoxomicin, which resulted in a marked accumulation of PanB and Pup~PanB, confirming PanB is a proteasome substrate (Fig. 3*D*) (3).

Discussion

In this work, we found CoaX, a pantothenate pseudokinase, modulates the depupylation of a specific enzyme, PanB. We identified CoaX through its interaction with Dop and obtained a high-resolution structure of the Pup-Dop-CoaX complex. Multiple-sequence alignment analysis found CoaX in proteasome-bearing species lack residues needed for ATPase activity compared to CoaX homologs in proteasome-lacking species. Thus, CoaX may be a pseudokinase in many organisms, and its role as a PanB depupylation regulator may be a widespread phenomenon. We also showed that pantothenate inhibits CoaX-activated depupylation of PanB in vitro and in *Mtb*. Collectively, our work identified a mechanism of feedback regulation where CoaX acts as a pantothenate sensor to modulate degradation of an enzyme that catalyzes a committed step in pantothenate synthesis (Fig. 4).

Trimers of CoaX dimers were previously described and dismissed as technical artifacts (39). However, our structure supports the biological relevancy of this structure. We speculate the specificity of CoaX activity on depupylation of PanB is achieved by an interaction between CoaX and Pup~PanB. It is possible that the Pup~PanB-CoaX-Dop complex is destabilized in the presence of pantothenate and/or ATP, leaving more PanB pupylated and vulnerable to degradation by proteasomes.

In *Mtb*, we expected that deletion of *coaX* would result in less efficient depupylation of Pup~PanB, leading to its degradation by proteasomes, and an overall lower amount of cellular PanB. However, PanB and PupP~PanB levels were elevated in a *coaX* strain compared to a parental strain. Based on the elevated transcript levels associated with genes encoding the pantothenate synthesis enzymes, we hypothesize that in the absence of *coaX*, PanB is constitutively degraded, leading to the increased expression of pantothenate synthesis genes by a yet-to-be determined mechanism.

All life forms must import or make pantothenate due to its essential role as a precursor of coASH synthesis. Pantothenate importers have been described in humans, yeast, malaria, and some bacteria (49–53); however, uptake mechanisms are unknown in *Mtb.* While pantothenate auxotrophs can survive in pantothenate-supplemented media, they are attenuated in mouse infection models (48). It is unknown if *Mtb* acquires pantothenate during human infections, or when its synthesis is most important for survival. Given the importance of coASH and its derivatives in numerous cellular processes,

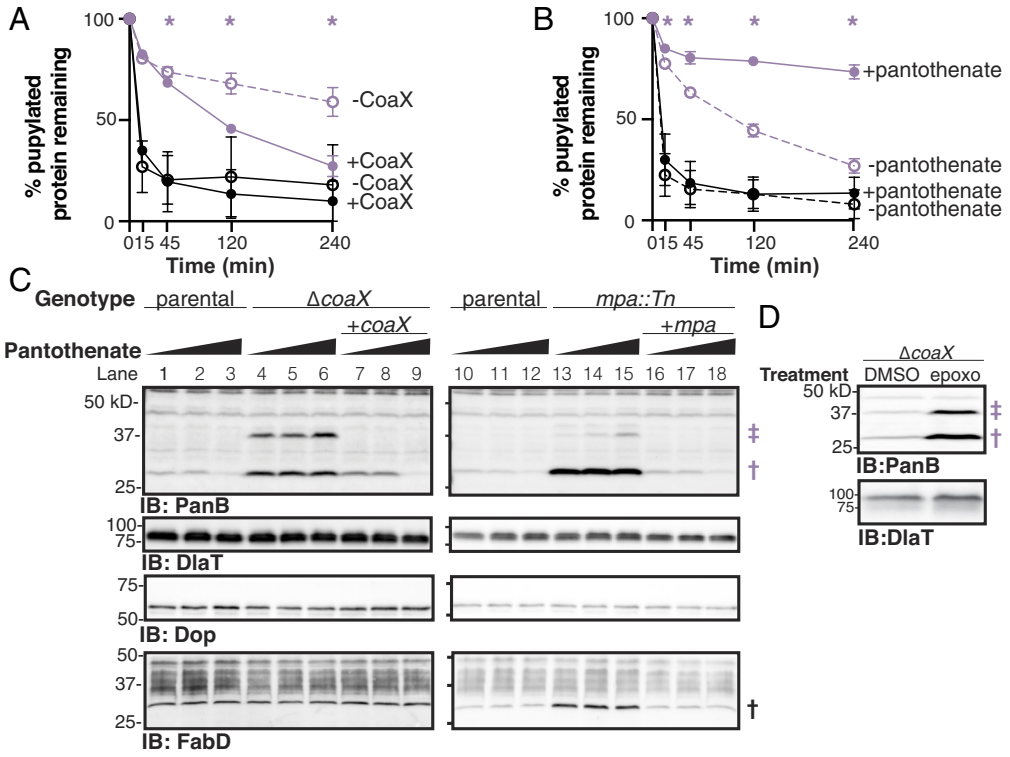

Fig. 3. Pup~PanB levels are regulated in a CoaX-, pantothenate-, and proteasome-dependent manner. (*A*) Percent of Pup~PanB (lavender) or Pup~FabD (black) remaining after 0, 15, 45, 120, and 240 min of depupylation in the presence (filled circles) or absence (open circles) of CoaX are graphed. Time points with statistically significant ($P < 0.05$) differences in percent of depupylated substrate remaining between reactions containing or lacking CoaX are indicated with color coordinated asterisks. (*B*) Percent Pup~PanB (lavender) or Pup~FabD (black) remaining after 0, 15, 45, 120, and 240 min of depupylation reactions containing CoaX in the presence (filled circles) or absence (open circles) of 1 mM pantothenate are graphed. Time points with statistically significant ($P < 0.05$) differences in percent depupylated substrate remaining between reactions containing or lacking pantothenate are indicated with color coordinated asterisks. (*C*) Immunoblots (IB) of lysates of Δ*coaX*, *mpa*::Tn, complemented strains, and parental controls grown in the presence of 0, 10, or 100 μM pantothenate are shown. Parental controls were transformed with empty vectors used for complementation constructs (*SI Appendix*, Table S1). IBs using DlaT or PanB antisera were performed on the same membranes. Endogenous Pup~PanB (‡, lavender), PanB (†, lavender), and FabD (†, black) are indicated. (*D*) IB against lysates of the Δ*coaX* strain treated for 24 h with DMSO (vehicle control) or 50 μM epoxomicin ("epoxo") are shown. IBs using PanB or DlaT (loading control) antisera were performed on the same membranes. Endogenous Pup~PanB (‡, lavender) and PanB (†, lavender) are indicated.

the existence of multiple mechanisms to tightly regulate pantothenate synthesis may be important (54). Along these lines, the dramatic accumulation of PanB in an *mpa* strain does not yield changes in pantothenate and other related metabolite levels (55), suggesting downstream regulatory mechanisms maintain homeostasis. Proteasomal turnover of PanB to nearly undetectable levels at steady state in culture

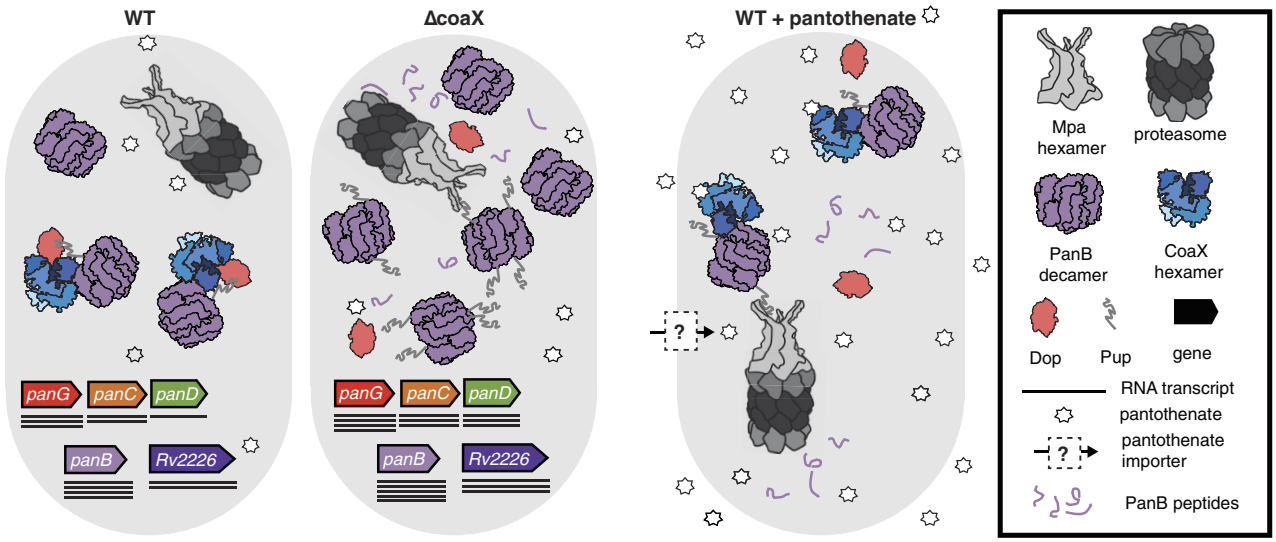

Fig. 4. Model of PanB regulation by CoaX, the Pup-proteasome system (PPS), and pantothenate. *Left*: Under standard culture conditions in WT *Mtb*, PanB levels are low, and CoaX is in complex with Dop. *Center*: Deletion of *coaX* leads to increased Pup~PanB and PanB levels. Pup~PanB is vulnerable to degradation by the proteasome. Additionally, RNA transcripts associated with pantothenate synthesis genes, including *panB*, are elevated in this strain compared to WT bacteria by an unknown mechanism. *Right*: Pantothenate supplementation of media leads to uptake by an unknown mechanism and decreased depupylation of Pup~PanB, rendering PanB more vulnerable to degradation by Mpa and the proteasome, lowering intracellular PanB levels. The specific effect of CoaX on Pup~PanB depupylation suggests CoaX and PanB interact directly, potentially even in the absence of Dop.

may indicate an underlying cost to pantothenate production. The presence of a specific depupylation regulator may also suggest that rapid induction of pantothenate synthesis is critical in some contexts. This model of regulation has parallels to the ubiquitin–proteasome system-dependent regulation of cholesterol metabolism by 3-hydroxy-3-methylglutaryl coenzyme A reductase in eukaryotes, where this enzyme is degraded in response to sterol levels (56).

While all proteasome-containing bacteria identified to date contain Pup, PafA, Dop, and Mpa homologs, *Corynebacterium glutamicum* stands out as a species containing all components of pupylation and proteasome activation (Mpa/ARC), but does not encode proteasome subunits (57). In *C. glutamicum*, ARC is thought to destabilize pupylated complexes of ferritin, a protein that forms a 24-subunit complex to sequester iron, by acting as an unfoldase (58). *C. glutamicum* does not encode CoaX, and its PanB is not known to be pupylated. However, IlvC, the sole ketopantoate reductase in this species, is a pupylated substrate (59, 60). Thus, Pup and ARC may regulate pantothenate synthesis even in the absence of CoaX and proteasome-mediated degradation by another mechanism.

Both pantothenate synthesis and PPS enzymes have previously been investigated as potential drug targets for *Mtb* [reviewed in (61) and (62)]. Focus on pantothenate biosynthesis has been motivated by the fact that humans do not make pantothenate and pantothenate synthesis is essential in *Mtb* under most laboratory conditions (48). Similarly, loss of any of the PPS enzymes yields dramatic virulence defects in mice infected with *Mtb* (2–6). A greater understanding of how pantothenate synthesis is regulated by the PPS or otherwise may offer new approaches for the successful development of antimicrobials targeting this pathway. Additionally, identification of PPS regulators has the potential to reveal new targets and pathways for drug development. Importantly, because this work shows how the pupylation status of a specific protein can be regulated, hypotheses to test how dozens, if not hundreds, of pupylated proteins are targeted for degradation can now be pursued.

Materials and Methods

Strains, Plasmids, Primers, and Culture Conditions. For a list of all strains, plasmids, and primers used in this work *SI Appendix*, Table S1. For detailed information on plasmid construction *SI Appendix*. All genes were amplified from *Mtb* H37Rv DNA unless specified otherwise. *E. coli* was cultured in Luria-Bertani broth (BD Difco) or on Luria-Bertani agar (Research Products International). *Mtb* and *Msm* were grown in Middlebrook 7H9 liquid broth (BD Difco) supplemented with 0.2% glycerol (Research Products International), 0.05% Tween-80, 0.5% bovine serum albumin fraction V (BSA, MilliporeSigma), 0.2% dextrose (VWR Chemicals BDH), and 0.085% sodium chloride ("7H9c"). For growth on agar, we used Middlebrook 7H11 (BD Difco) supplemented with 0.5% glycerol and 10% BBL Middlebrook Oleic Albumin Dextrose Catalase Growth Supplement (BD Difco). For *E. coli*, we used antibiotics as follows: 100 μg/ml kanamycin, 150 μg/ml hygromycin, 50 μg/ml streptomycin sulfate, or 200 μg/ml ampicillin sodium salt. *E. coli* and *Msm* were grown at 37 °C, shaking or rotating, and optical density ("OD") measured at 600 nm (OD_{600}) or 580 nm (OD_{580}), respectively. For *Mtb* and *Msm,* selection was performed using kanamycin sulfate 50 μg/ml, hygromycin B (Corning) 50 μg/ml, or streptomycin sulfate (Acros) 25 μg/ml. For pantothenate supplementation, D-calcium pantothenate was dissolved at 100 μM in water, syringe filter sterilized (Corning, 0.45 μM, nylon), and diluted into 7H9c. All *Mtb* cultures were grown static at 37 °C, and growth monitored at OD_{580}. Bacteria harvested for immunoblotting or mass spectrometry were washed with Dulbecco's phosphate-buffered saline ("PBS," Corning) and 0.05% Tween-80 ("PBS-T") prior to lysis. To inhibit proteasome activity, we used epoxomicin (Selleckchem) as previously described (3).

For growth curves in minimal media, *Mtb* strains were grown to mid-log phase, washed thrice with PBS-T, and resuspended at OD_{580} 0.05 in Sauton's broth [3.7 mM potassium phosphate, monobasic; 2.4 mM magnesium sulfate heptahydrate; 30 mM L-(+)-asparagine monohydrate; 3.5 mM zinc sulfate; 9.5 mM citric acid trisodium salt dihydrate (Acros Organics); 6.0% glycerol; 0.005% ferric ammonium citrate (MP Biochemicals); 0.05% Tween-80] or Proskauer-Beck broth [0.5% potassium phosphate monobasic, 0.06% magnesium sulfate heptahydrate, 1.5% glycerol, 0.25% magnesium citrate, dibasic anhydrous (Chem-Impex International), 0.05% Tween 80, and 10 mM L-(+)-asparagine monohydrate].

Protein Analysis. *Mtb* lysates were prepared by bead beating in 50 mM Tris-HCl pH8, 1 mM EDTA pH8, as previously described (28). Lysates for immunoprecipitation were filter sterilized with 0.22 nylon syringe filters (CELLTREAT). Lysates made for mass spectrometry were filtered with SpinX centrifuge tube filters (Costar). Immunoblots were performed with monoclonal antibodies to Pup (4, 28) or polyclonal antibodies to Dop (12), DlaT (63), PrcB (22), or FabD (7) as previously described. Monoclonal ANTI-FLAG M2 antibody (Sigma Aldrich) was used according to the manufacturer's instructions. For polyclonal antibody production, CoaX and $_{FLAG}PanB_{his}$ were purified from *E. coli* under native conditions using Ni-NTA agarose (Qiagen). Elutions were pooled and dialyzed overnight at 4 °C in PBS and concentrated with Amicon Ultracel 3 K filters (Millipore) for immunization of rabbits by Covance (Denver, PA). For additional immunoblotting procedures *SI Appendix, Supplementary Experimental Procedures*.

Protein Purification. *Msm* Dop_{C438S} was used for all in vitro depupylation assays and purified as described previously (64). Protein was stored in 50 mM $NaPO_4$ pH 8, 10 mM $MgCl_2$, 150 mM NaCl, and 20% glycerol and flash frozen with an ethanol-dry ice bath for storage at −80 °C. Protein concentrations were quantified by Bradford assay using Bio-Rad Protein Assay Dye Reagent Concentrate according to the manufacturer's instructions. For CryoEM analysis, CoaX was purified from the pETDUET-$_{his}pup_{91}$-*coaX*-$dop_{MsmC438S}$ construct and the CoaX+ Dop_{Msm} + Pup complex was purified from pETDUET-$_{TwinStrep}pup_{91}$-*coaX*-$dop_{MsmC438S}$ construct. In brief, N-terminally truncated and tagged Pup ($_{his6}Pup_{91}$ or $_{TwinStrep}Pup_{91}$) was coproduced in *E. coli* with Dop_{Msm} and $GroESL_{Ecoli}$. These strains were grown to OD_{600} 0.4 to 1.0, induced with 0.6 mM isopropyl ß-D-1-thiogalactopyranoside (IPTG, IBI Scientific), and grown for another 4 to 6 h at 37°C. Untagged Dop_{Msm} was purified by interaction with $_{his}Pup_{91}$ using Ni-NTA agarose (Qiagen) as previously published (64) or $_{TwinStrep}Pup_{91}$ on Strep-TactinXT 4Flow High Capacity Resin (IBI Scientific) and further purified by SEC using a Superose™ 6 10/300 GL column and ÄKTA Pure Protein Purification System (Cytiva). Purification of CoaX in the absence of Dop was performed similarly, but cultures were induced with 1 mM IPTG. SEC fractions of each protein were concentrated and buffer exchanged with Amicon Ultra 10 kD MWCO Centrifugal Filters (Millipore Sigma) according to the manufacturer's instructions.

$_{Myc}Pup{\sim}_{FLAG}PanB_{his}$, and $_{Myc}Pup{\sim}_{FLAG}FabD_{his}$ were purified from proteasome-lacking *Msm* for depupylation assays as previously described (65). $_{Myc}Pup{\sim}_{FLAG}PanB_{his}$ was purified in complex with $_{FLAG}PanB_{his}$ due to apparent heterogeneous pupylation of the PanB decamer (46).

For kinase and DSF assays, $CoaA_{his}$, $CoaX_{his}$, and $CoaX_{DM\_his}$ were produced for purification by transforming corresponding pET28a-based plasmids into BL21(DE3). Single colony transformants were inoculated into 10 ml LB media supplemented with kanamycin, grown overnight, and subcultured into 1 l LB broth the following morning. Upon reaching OD_{600} 0.5 to 0.7, they were cold shocked and induced with 1 mM IPTG overnight at 18 °C. The cell pellet was obtained by centrifugation and resuspended in 50 mM Tris-HCl pH 8.0, 300 mM NaCl, 10% glycerol, and 25 mM imidazole. Cells were lysed by French Press Cell Disruptor, icing between cycles. Soluble lysate was loaded onto a Ni-NTA agarose column, proteins eluted with 300 mM imidazole, and applied to Gravity PD-10 Desalting columns (Cytiva) used to change buffer according to the manufacturer's instructions.

Cryo-EM Sample Preparation, Screening, and Data Collection. SEC fractions were screened by negative-stain electron microscopy to assess sample quality and homogeneity. For negative stain electron microscopy, protein sample was applied to freshly glow-discharged carbon-coated 400 mesh copper grids (Ted Pella Inc., cat. #01754-F) and subsequently blotted with filter paper. Immediately after blotting, a 0.75% uranyl formate solution was applied for staining, followed by five rounds of stain application and blotting. Grids were imaged on a Talos L120C TEM (FEI) equipped with a 4 K. 4 K OneView camera (Gatan).

For cryo-EM of CoaX, fractions of interest were concentrated to 0.01 mg/ml in 50 mM Tris-HCl pH 8.0, 150 mM NaCl, and 1 mM DTT. Continuous carbon

grids (Quantifoil R 2/2 on Cu 300 mesh grids + 2 nm Carbon, Quantifoil Micro Tools C2-C16nCu30-01) were glow-discharged for 5 s in an easiGlow Glow Discharge Cleaning System (Ted Pella Inc.). 3.5 μl sample was applied to the glow-discharged grid. Using a Vitrobot Mark IV, grids were blotted for 3 s at 22 °C with 100% chamber humidity and plunge-frozen into liquid ethane. Clipped grids were screened at the NYU Cryo-EM Laboratory on a Talos Arctica operated at 200 kV equipped with a K3 camera (Gatan). Grids were selected for data collection based on ice quality and particle distribution. Selected grids were imaged at NYU Cryo-EM Laboratory on a Krios-3Gi operated at 300 kV with a K3 camera (Gatan) and an energy filter slit width of 20 eV. Superresolution movies were collected using Leginon v3.6 at a nominal magnification of 105,000×, corresponding to a superresolution pixel size of 0.41275 Å (or a nominal pixel size of 0.8255 Å after binning by 2). Movies were collected at a dose rate of 26.95 e-/Å^2/s with a total exposure of 1.80 s, for an accumulated dose of 48.51 e-/Å^2. Intermediate frames were recorded every 0.05 s, 40 frames per micrograph. A total of 7,913 images were collected at a nominal defocus range of 0.8 – to 2.5 μm.

For cryo-EM of CoaX+ Dop$_{Msm}$ + Pup$_{91}$, fractions of interest were concentrated to ~2 mg/ml in 50 mM Tris-HCl pH 8.0, 150 mM NaCl, and 1 mM DTT. C-flat grids (Protochip, CF-1.2/1.3-4AU-50) were glow-discharged for 30 s in an easiGlow Glow Discharge Cleaning System. Using a Vitrobot Mark IV, grids were blotted for 3 s at 22 °C with 100% chamber humidity and plunge-frozen into liquid ethane. Clipped grids were screened at the NYU Cryo-EM Laboratory on a Talos Arctica microscope. Data were collected on optimal grids at NYU Cryo-EM Laboratory on a Krios-3Gi operated at 300 kV with a K3 camera (Gatan) and an energy filter slit width of 20 eV. Superresolution movies were collected using Leginon v3.6 at a nominal magnification of 105,000×, corresponding to a superresolution pixel size of 0.41275 Å (or a nominal pixel size of 0.8255 Å after binning by 2). Movies were collected at a dose rate of 27.15 e-/Å^2/s with a total exposure of 1.80 s, for an accumulated dose of 48.87 e-/Å^2. A total of 11,015 images were collected at a nominal defocus range of 0.8 to 2.5 μm.

Cryo-EM Data Processing for CoaX. The Krios dataset was split into eight batches of 1,000 movies and processed in cryoSPARC v4.31 (61), as described in *SI Appendix*, Fig. S3. Dose-fractionated movies were gain-normalized, drift-corrected, summed, and dose-weighted using the cryoSPARC Patch Motion module (max resolution alignment: 3 Å, output F-crop factor: 1/2). The contrast transfer function was estimated for each summed image using cryoSPARC Patch CTF (amplitude contrast: 0.07, maximum resolution: 1.64 Å, maximum search defocus: 50,000 Å).

Micrographs from each batch were picked using cryoSPARC Blob Picker (min particle diameter: 100 Å, max particle diameter: 200 Å, max # of local maxima to consider: 1,000) and extracted using Extract From Micrographs module (extraction box size: 256 px, Fourier crop to box size: 64 px) resulting in 4,199,792 total particles across the eight batches. For each batch, extracted particles were sorted using 2D Classification (N = # of classes = 50, remove duplicate particles). From one of the eight batches, particles from "junk" classes were selected and processed using cryoSPARC Ab initio Reconstruction (N = 3, # of particles to use: 100,000) to generate three decoy models (Decoy 1, Decoy 2, and Decoy 3) for downstream particle curation using cryoSPARC Heterogenous Refinement. Particles from well-defined classes were selected from each batch, combined (1,742,997 particles total), and sorted by another round of 2D Classification (N = 50). Particles from well-resolved 2D classes (1,194,966 particles) were selected and re-extracted using Extract From Micrographs module (Extraction box size: 256 px, no binning).

Extracted particles were processed using cryoSPARC Ab initio Reconstruction (N = 3, # of particles to use: 100,000, max res: 7 Å, initial resolution: 9 Å) to generate initial 3D models [Model 1 (22,953 particles), Model 2 (19,586 particles), Model 3 (57,461 particles)]. Extracted particles were further curated with five rounds of Heterogeneous Refinement [N = 6 classes, templates = (1) Model 1, (2) Model 2, (3) Model 3, (4) Decoy 1, (5) Decoy 2, (6) Decoy 3], in which particles sorted into Models 1, 2, and 3 were used as input for the next round and particles in Decoys 1, 2, and 3 were discarded and not further processed. Multiple rounds of Heterogeneous Refinement were performed (round 1: 990,417 particles, round 2: 899,837 particles, round 3: 838,692 particles, round 4: 798,094 particles, round 5: 774,783 particles) until less than 3% of input particles were sorted into Decoy classes. Curated particles were classified using Heterogeneous Refinement [N = 3, templates = (1) Model 3, (2) Model 3, (3) Model 3], revealing two distinct classes of *Mtb* CoaX: hexamer (Ref 1) and tetramer (Ref 2), which were used as references for downstream particle curation.

To sample more views of the hexamer and tetramer, particles from Models 1, 2, and 3 were each sorted by 2D classification (N = 50) and particles from 2D classes containing unique views were selected. Particles from the five different views were separately trained within the Topaz Train module (62) in cryoSPARC (expected # of particles: 1,000, model architecture: ResNet16). After training, particles were picked using the trained Topaz model and extracted (extraction box size: 256 px, Fourier crop to box size: 64 px). Particles from the five separate Topaz pickings (view1: 5,435,920 particles; view2: 3,495,604 particles; view3: 5,978,176 particles; view4: 7,226,460 particles; view5: 5,963,535 particles) were aligned using 2D Classification (N = 50), combined, and duplicate particle picks were removed. Particles were re-extracted using Extract From Micrographs module (extraction box size: 256 px, no binning), resulting in 8,929,726 particles.

Extracted particles were curated by running four rounds of Heterogeneous Refinement [N = 5, templates = (1) Ref 1, (2) Ref 2, (3) Decoy 1, (4) Decoy 2, (5) Decoy 3], in which particles sorted into Ref 1 and Ref 2 were used as input for the next round and particles in Decoys 1, 2, and 3 were discarded and not further processed. Multiple rounds of Heterogeneous Refinement (round 1: 4,653,022 particles, round 2: 3,412,231 particles, round 3: 2,347,502 particles, round 4: 2,154,528 particles) were performed until resolution of Ref1 and Ref2 did not improve further. After removing remaining duplicates (alignment3D), the 1,285,898 curated particles in the hexamer class (Ref 1) and the 771,380 curated particles in the tetramer class (Ref 2) were refined using cryoSPARC Non-Uniform Refinement (63) (initial lowpass resolution: 15 Å) generating density maps with average resolutions of 2.59 Å-resolution and 2.81 Å, respectively.

Cryo-EM Data Processing for CoaX + Dop$_{Msm}$ + Pup$_{91}$. The Krios dataset was split into twelve batches of 1,000 movies and processed in cryoSPARC v4.5.1 (61), as described in *SI Appendix*, Fig. S1. Dose-fractionated movies were gain-normalized, drift-corrected, summed, and dose-weighted using the cryoSPARC Patch Motion module (max resolution alignment: 3 Å, output F-crop factor: 1/2). The contrast transfer function was estimated for each summed image using cryoSPARC Patch CTF (amplitude contrast: 0.07, maximum resolution: 1.65 Å, maximum search defocus: 50,000 Å).

Using a subset of 1,000 micrographs, particles were initially picked using cryoSPARC Blob Picker (min particle diameter: 100 Å, max particle diameter: 200 Å, max # of local maxima to consider: 2,000) and extracted using Extract From Micrographs module (extraction box size: 360 px, Fourier crop to box size: 90 px). Extracted particles were sorted using two rounds of 2D Classification (N = # of classes = 50, remove duplicate particles), selecting for well-resolved 2D classes. 2D classes of different view angles were used as templates for cryoSPARC Template Picker (particle diameter: 200 Å, min separation distance: 0.2 diameters, max # of local maxima to consider: 2,000) to pick from a subset of 1,000 micrographs. Picked particles were extracted using the Extract From Micrographs module (extraction box size: 360 px, Fourier crop to box size: 90 px) and subjected to two rounds of 2D Classification (N = # of classes = 50, remove duplicate particles), to sort out unique viewing angles (4 total) of the complex for Topaz Train. Particles from "junk" classes were selected (580,562 particles) and processed using cryoSPARC Ab initio Reconstruction (N = 3, max resolution 7 Å, initial resolution: 9 Å) to generate three decoy models (Decoy 1, Decoy 2, and Decoy 3) for downstream particle curation using cryoSPARC Heterogenous Refinement. Curated particles for each unique view were used to train a separate Topaz picking model through the Topaz Train module (expected # of particles: 1000, use pretrained initialization, model architecture: ResNet8). The four Topaz training models were applied to pick particles from the subset of 1,000 micrographs to generate an initial 3D model. Picked particles (485,131 particles) were extracted using the Extract From Micrographs module (extraction box size: 360 px, Fourier crop to box size: 90 px), subjected to 2D classification (N = 50, remove duplicate particles), and particles from well-resolved classes were selected. Selected 197,245 particles were re-extracted (extraction box size: 360 px, no binning) and used for Ab initio Reconstruction (N = 3, # of particles to use: 100,000, max res: 7 Å, initial resolution: 9 Å) to generate an initial 3D reconstruction of the complex (denoted as "Reference").

Each batch of micrographs was subsequently picked using the four Topaz picking models, and particles were extracted using Topaz Extract and Extract from

Micrographs modules (extraction box size: 360 px, Fourier crop to box size: 90 px). Particles from each batch (22,780,331 total particles across the twelve batches) were 2D classified (N = 50, remove duplicate particles) to remove duplicate picks and then re-extracted (extraction box size: 360 px, no binning). Extracted particles for each batch were curated by running two rounds of Heterogeneous Refinement [N = 4, templates = (1) Reference, (2) Decoy 1, (3) Decoy 2, (4) Decoy 3], in which particles sorted into Reference were used as input for the next round until the resolution of the "Reference" reconstruction did not improve further. Curated particles for each batch were refined using cryoSPARC Non-Uniform Refinement (minimize over per-particle, optimize per-particle defocus, optimize per-group CTF parameters) to perform per-particle Global and Local CTF estimations. From each batch, refined particles were further curated using supervised 3D classification using cryoSPARC Ab-initio Reconstruction (N = 3, max res: 7 Å, initial resolution: 9 Å) to remove higher-order oligomers and overrepresented orientations for a more isotropic 3D reconstruction of the CoAXhexamer + Dop*Msm* + Pup_{91} complex. Curated particles from each batch were refined using cryoSPARC Non-Uniform Refinement (minimize over per-particle) followed by cryoSPARC Reference Based Motion Correction.

Corrected particles from the twelve batches were combined (2,336,294 total particles) and were refined together using cryoSPARC Non-Uniform Refinement, resulting in a consensus 3D reconstruction at 1.98 Å-resolution. Signal subtraction and cryoSPARC Local Refinement was performed to improve the density for Dop and Pup_{91}, resulting in a locally refined map at 2.12 Å-resolution. The locally refined maps of Dop and Pup_{91} were combined with the consensus map using PHENIX "Combine Focused Map" (66) to generate a composite map at 2.04 Å-resolution for model building. The resolution of the composite map was estimated by generating composite half maps and calculating the Fourier shell correlation.

Model Building and Refinement. For the initial model of CoaX, we used AlphaFold2 (64) to generate a monomer of CoaX through ColabFold (65). The predicted CoaX monomers were manually fit as rigid bodies into the cryo-EM maps of the CoaX hexamer and tetramer using ChimeraX (67). CoaX hexamer and tetramer models were further refined using real-space refinement in PHENIX v1.20.19 (68). The refined models were manually inspected in COOT v0.8.9.2 (69) to assess the overall fit for the Cα backbone and side chains of each CoaX protomer into the maps. These models were iteratively inspected, manually rebuilt in COOT, and refined in PHENIX until completion. Final model refinements were performed using PHENIX with global minimization, Ramachandran restraints, secondary structure restraints, and nonbond weight set at 200.0. The final model for the CoaX hexamer and tetramer is nearly complete apart from the C-terminal regions of each CoaX promoter (residues 261 to 272). These residues were not modeled since they were not well-resolved in the cryo-EM maps.

To model the CoaX + Dop_{Msm} + Pup_{91} complex, the CoaX hexamer model and an AlphaFold2 prediction of Dop_{Msm} bound to Pup_{91} were manually docked into the cryo-EM map within ChimeraX. Each protein chain was fitted into the map as a rigid body within ChimeraX. In each CoaX protomer, residues 162 to 175 form a loop that makes up part of the interface between two CoaX dimers with chain B interacting with chain F, chain A interacting with chain C, and chain D interacting with chain E. These loops were resolved to varying extents. Among the six loops, the loop in chain B was best resolved in the map and therefore, fully modeled. This loop was used to guide the modeling of the other five CoaX loops. The loop in chain F that interacts with the loop of chain B appears mostly disordered, thus residues 163 to 169 were not modeled. The loops in chain A and C (encompassing residues 162 to 175) appear to adopt an ordered and disordered state, with the ordered state of chain A and C occupying the same physical space. Therefore, both conformations were modeled in both chains at 50% occupancy. The loops in chain D and E were modeled similarly to chain A and C. The model for the complex was refined through iterations of real-space refinement in PHENIX v1.20.19 and manually inspected in COOT v0.8.9.2. Hydrogens were added using PHENIX "ReadySet" and waters added and further inspected using COOT. Final model refinements were performed using PHENIX with global minimization, occupancy, Ramachandran restraints, secondary structure restraints, and nonbond weight set at 200.0. The final model for the CoaX hexamer bound to Dop and Pup_{91} lacked several regions that were not modeled due to poor density: residues 262 to 272 of each CoaX promoter, 40 to 83 and 428 to 498 of Dop, and 1 to 39 of Pup_{91}.

Quantification and statistical analyses for model refinement and validation on deposited models were extracted from the results of the real_space_refine algorithm in PHENIX (68) as well as MolProbity (70) and EMringer (71). Structural alignments and associated RMSD values were calculated using PyMOL (Schröodinger, LLC). The local resolution of the cryo-EM maps was estimated using cryoSPARC Local Resolution (61). FSCs that were calculated in cryoSPARC were plotted in Prism v10 (GraphPad). Directional 3DFSCs were calculated using 3DFSC (72) and directional view plots were generated in cryoSPARC. Figs. were generated with PyMOL (Schröodinger, LLC) and ChimeraX (67). Protein–protein interfaces and interactions were calculated using PDBePISA (41) PDBsum (68).

Mass Spectrometry to Identify Dop Binding Partners and Characterize the Proteome of WT and Δ*coaX* Strains. Dop tagged with a tandem affinity purification (TAP) tag (C-terminal FLAG-tag followed by hexahistidine tag), Dop_{TAP}, was immunoprecipitated from *Mtb* lysed in 50 mM NaH_2PO_4 pH 7.4, 100 mM NaCl by batch purification with EZview Red ANTI-FLAG M2 Affinity gel and eluted with 3XFLAG peptide according to the manufacturer's instructions (Sigma-Aldrich). Elutions were examined by SDS–PAGE on a 10% acrylamide gel and Coomassie brilliant blue staining. The dominant binding partner was excised from the gel and processed by the Proteomics Laboratory at NYU Langone.

To globally identify Dop and PafA binding partners, Dop_{TAP} and $PafA_{TAP}$ (C-terminally tagged identically to Dop_{TAP}) were immunoprecipitated from quadruplicate *Mtb* cultures using anti-FLAG affinity gel as described above. Elutions were analyzed by mass spectrometry.

Total proteomics was performed on lysates extracted from four cultures of WT and Δ*coaX* strains. Lysates were prepared by bead beating in 100 mM Tris pH 8.0, 1 mM EDTA, and filter sterilized using 0.22 μ nylon filters (CELLTREAT).

Pantothenate Kinase Activity Assays. Pantothenate kinase activity was measured using ADP-Glo Kinase assay (Promega) according to the manufacturer's instructions. To investigate kinases' activity, ADP formed by in vitro reactions is converted to ATP, which is used to generate light by a subsequent luciferase reaction. Luminescence measured by plate reader is therefore correlated with the abundance of ADP generated by the initial in vitro reaction, yielding a quantitative, but indirect, indication of ATPase activity.

Recombinant CoaA, CoaX, and $CoaA_{DM}$ were incubated with increasing concentrations of pantothenate for 30 min in 50 mM HEPES, 25 mM KCl, 20 mM $MgCl_2$, 0.1 M EDTA, 2 mM DTT, 0.002% Brij-35, and 5 mM ATP as previously described (36). Reactions were quenched by addition and incubation with ADP Glo Reagent. Kinase Detection Reagent was then added and luminescence measured with SpectraMax iD5 Microplate reader. Graphs were generated with Prism (Graphpad) and represent results from duplicate experiments.

Differential Fluorimetry Scanning. 10 μM of purified CoaX was mixed with 5 μl SYPRO Orange (Thermo Fisher Scientific) in 50 mM Tris-HCl, 300 mM NaCl, and 10% glycerol. Reactions included 0 to 10 mM ATPγS, 0 to 4 mM pantothenate, or 4 mM pantothenate with 0 to 10 mM ATPγS. Reactions were conducted in a 96-well microplate, total volume 25 μl, and monitored using a BioRad CFX 96 qPCR instrument equipped with a FRET channel.

Evolutionary Analysis of CoaX Sequences. Homologs of CoaX were identified using the *Mtb* CoaX amino acid sequence (P9WPA1.1) as query in a PSI-BLAST search (73) against the nonredundant protein database from National Center for Biotechnology Information that was clustered down to 50% identity (nr50). For TaxID and CoaX accession numbers *SI Appendix*, *Supplementary Experimental Procedures*. An MSA was generated with FAMSA (74) and adjusted based on structural data.

To determine the presence of Type I and Type II PanK enzymes, PSI-BLAST searches were performed on the nr50 database using *Mtb* CoaA(CCP43845.1) and *Staphylococcus aureus* PanK (NP_646871.1) as queries, respectively. The NCBI TaxIDs of species in the CoaX alignment were used to filter results.

RNAseq. RNA was extracted from four cultures of MHD761 (H37Rv pMV306.strep), MHD1845 (Δ*coaX*::*hyg* pMV306.strep), and MHD1846 (Δ*coaX*::*hyg* pMV306.strep-*coaX*) as previously described (75). Library preparation (using Ribozero plus) and paired-end 50 bp sequencing (on an SP 100 Cycle Flow Cell v1.5 using an Illumina NovaSeq 6000) was conducted by the NYU Langone Genome Technology Center. Reads were mapped to the H37Rv genome [RefSeq identifier GCF_000195955.2 with *socAB* annotation added as previously

described (76)] using Bowtie2 v2.4.1 (77) and sorted using samtools v1.13 (78). Aligned read counts were extracted using the featureCounts command in Subread v2.0.1 (79). Normalization and differential expression analysis was performed using DESeq2 v1.40.2 (80) defaults using R (81), RStudio v2023.9.0.463, and tidyverse v2.0.0 (82). Genes with Wald test *p*-values adjusted for multiple hypothesis testing (Benjamini and Hochberg) of less than 0.1 were considered significant. Normalized read counts were plotted with Prism v10 for figure.

Mouse Infections. Six- to eight-week-old female mice (C57BL6/J, Jackson Laboratories) were infected with WT, Δ*coaX*, or the complemented strain as previously described (5) with the approval of the New York University Institutional Animal Care and Use Committee. Mice were humanely euthanized and organs harvested at days 1, 22, and 56, and 196 d (n = 8 to 10 over two independent experiments) following infection. All procedures were performed with the approval of the New York University Institutional Animal Care and Use Committee. Lungs were harvested at all time points and spleens were harvested at all time points except day 1.

Depupylation Assays. Purified pupylated substrates ($_{Myc}$Pup~$_{FLAG}$PanB$_{Mtb_his}$ or $_{Myc}$Pup~$_{FLAG}$FabD$_{Mtb_his}$) were mixed with Dop$_{Msm}$ at a 4:1 ratio by protein concentration in 50 mM $NaPO_4$, 10 mM $MgCl_2$, 150 mM NaCl, 1 mM DTT, 5 mM ATP, and 10% glycerol (total volume of 100 μl) on ice. $_{Myc}$Pup~$_{FLAG}$PanB$_{his}$ depupylation reactions contained 2 μg of purified substrate; $_{Myc}$Pup~$_{FLAG}$FabD$_{his}$ reactions contained 0.9 μg. When included, CoaX was mixed at a ratio of 2:1 with Dop by concentration, prior to the addition of substrate. When included, 1 mM pantothenate was premixed with reactions prior to the addition of substrate. A sample was collected at start and reactions incubated at 30 °C in a ThermoMixer C (Eppendorf). Additional samples were collected at 15, 45, 120, and 240 min. Depupylation of $_{Myc}$Pup~$_{FLAG}$PanB$_{his}$ was analyzed by SDS-PAGE and staining with ProtoStain Blue (National Diagnostics) according to the manufacturer's instructions. Depupylation of $_{Myc}$Pup~$_{FLAG}$FabD$_{his}$ was analyzed using Pierce Silver Stain for Mass Spectrometry according to the manufacturer's instructions using Glacial Acetic Acid and 190 proof Ethanol (Decon Labs). All gels were scanned and band density measured with Fiji (Image J). Pupylated protein remaining at each time point was calculated as a ratio of the proportion of pupylated protein at each time point relative to the starting proportion of pupylated protein. Results were graphed and Mann–Whitney tests performed in Prism v10.

Data, Materials, and Software Availability. Raw sequence data and inferred gene features are available from the NCBI Gene Expression Omnibus under the accession number GSE260838 (83). All other data are included in the article and/or supporting information.

ACKNOWLEDGMENTS. We thank A. Darwin for reading a draft version of this manuscript and S. Zhang for making the TAP-tagged plasmids. We thank J. Ilmain for assistance with SEC and negative stain EM. We thank the Office of Science & Research High-Containment Laboratories at NYU Grossman School of Medicine for their support in the completion of this research. We thank W. Rice, B. Wang, H. Juang for assistance with cryo-EM grid screening and microscope operation. EM data processing used computing resources at the HPC Facility at NYU, and we thank the members of the HPC team for high-performance computing support. K.H.D. is funded by NIH grant AI088075. G.B. and D.C.E. are funded by NIH grant AI174646. L.A. and L.M.I. are supported by the National Library of Medicine Intramural Research Program at the NIH. K.Y.R. is supported by NIAID P01 AI143575 and BMGF INV-204250. S.C.K. was supported in part by a Public Health Service Institutional Research Training Award T32 AI007180. J.C. is a fellow of The Jane Coffin Childs Memorial Fund for Medical Research. This investigation has been aided by a grant from The Jane Coffin Childs Memorial Fund for Medical Research. Some of the work was performed at NYU Langone Health's Cryo-Electron Microscopy Laboratory (RRID: SCR_019202), which is partially supported by the Laura and Isaac Perlmutter Cancer Center Support Grant NIH/NCI P30CA016087.

Author affiliations: [a]Department of Microbiology, New York University Grossman School of Medicine, New York, NY 10016; [b]Department of Cell Biology, New York University School of Medicine, New York, NY 10016; [c]Department of Medicine, Weill Cornell Medicine, New York, NY 10021; [d]Computational Biology Branch, National Center for Biotechnology Information, National Library of Medicine, NIH, Bethesda, MD 20894; [e]Antimicrobial-Resistant Pathogens Program, New York University Grossman School of Medicine, New York, NY 10016; [f]Microbial Computational Genomic Core Lab, New York University Grossman School of Medicine, New York, NY 10016; and [g]Department of Biology, Johns Hopkins University, Baltimore, MD 21218

Author contributions: S.C.K., J.C., D.C.E., G.B., K.Y.R., and K.H.D. designed research; S.C.K., J.H.Y., J.C., K.N., L.M.I., L.A., and G.B. performed research; S.C.K., J.H.Y., J.C., K.N., L.M.I., G.P., N.M.S., A.P., L.A., D.C.E., G.B., K.Y.R., and K.H.D. analyzed data; and S.C.K., J.H.Y., J.C., K.N., L.M.I., A.P., L.A., D.C.E., G.B., K.Y.R., and K.H.D. wrote the paper.

1. World Health Organization, *Global Tuberculosis Report 2022* (Geneva, 2022).
2. K. H. Darwin, G. Lin, Z. Chen, H. Li, C. F. Nathan, Characterization of a Mycobacterium tuberculosis proteasomal ATPase homologue. *Mol. Microbiol.* **55**, 561–571 (2005).
3. M. J. Pearce *et al.*, Identification of substrates of the Mycobacterium tuberculosis proteasome. *EMBO J.* **25**, 5423–5432 (2006).
4. F. A. Cerda-Maira *et al.*, Molecular analysis of the prokaryotic ubiquitin-like protein (Pup) conjugation pathway in Mycobacterium tuberculosis. *Mol. Microbiol.* **77**, 1123–1135 (2010).
5. K. H. Darwin, S. Ehrt, J. C. Gutierrez-Ramos, N. Weich, C. F. Nathan, The proteasome of Mycobacterium tuberculosis is required for resistance to nitric oxide. *Science* **302**, 1963–1966 (2003).
6. S. Gandotra, D. Schnappinger, M. Monteleone, W. Hillen, S. Ehrt, In vivo gene silencing identifies the Mycobacterium tuberculosis proteasome as essential for the bacteria to persist in mice. *Nat. Med.* **13**, 1515–1520 (2007).
7. R. A. Festa *et al.*, Prokaryotic ubiquitin-like protein (Pup) proteome of Mycobacterium tuberculosis [corrected]. *PLoS One* **5**, e8589 (2010).
8. M. J. Pearce, J. Mintseris, J. Ferreyra, S. P. Gygi, K. H. Darwin, Ubiquitin-like protein involved in the proteasome pathway of Mycobacterium tuberculosis. *Science* **322**, 1104–1107 (2008).
9. K. E. Burns, W.-T. Liu, H. I. Boshoff, P. C. Dorrestein, C. E. Barry, Proteasomal protein degradation in Mycobacteria is dependent upon a prokaryotic ubiquitin-like protein. *J. Biol. Chem.* **284**, 3069–3075 (2009).
10. F. Striebel *et al.*, Bacterial ubiquitin-like modifier Pup is deamidated and conjugated to substrates by distinct but homologous enzymes. *Nat. Struct. Mol. Biol.* **16**, 647–651 (2009).
11. F. Imkamp *et al.*, Deletion of dop in Mycobacterium smegmatis abolishes pupylation of protein substrates in vivo. *Mol. Microbiol.* **75**, 744–754 (2010).
12. K. E. Burns *et al.*, "Depupylation" of prokaryotic ubiquitin-like protein from mycobacterial proteasome substrates. *Mol. Cell* **39**, 821–827 (2010).
13. F. Imkamp *et al.*, Dop functions as a depupylase in the prokaryotic ubiquitin-like modification pathway. *EMBO Rep.* **11**, 791–797 (2010).
14. K. E. Burns, M. J. Pearce, K. H. Darwin, Prokaryotic ubiquitin-like protein provides a two-part degron to Mycobacterium proteasome substrates. *J. Bacteriol.* **192**, 2933–2935 (2010).
15. F. Striebel, M. Hunkeler, H. Summer, E. Weber-Ban, The mycobacterial Mpa-proteasome unfolds and degrades pupylated substrates by engaging Pup's N-terminus. *EMBO J.* **29**, 1262–1271 (2010).
16. D. Li *et al.*, Structural basis for the assembly and gate closure mechanisms of the Mycobacterium tuberculosis 20S proteasome. *EMBO J.* **29**, 2037–2047 (2010).
17. G. Lin *et al.*, Mycobacterium tuberculosis prcBA genes encode a gated proteasome with broad oligopeptide specificity. *Mol. Microbiol.* **59**, 1405–1416 (2006).
18. T. Wang *et al.*, Structural insights on the Mycobacterium tuberculosis proteasomal ATPase Mpa. *Structure* **17**, 1377–1385 (2009).
19. K. Hu *et al.*, Proteasome substrate capture and gate opening by the accessory factor PafE from Mycobacterium tuberculosis. *J. Biol. Chem.* **293**, 4713–4723 (2018).
20. M. Kavalchuk, A. Jomaa, A. U. Müller, E. Weber-Ban, Structural basis of prokaryotic ubiquitin-like protein engagement and translocation by the mycobacterial Mpa-proteasome complex. *Nat. Commun.* **13**, 276 (2022).
21. S. C. Kahne, K. H. Darwin, Structural determinants of regulated proteolysis in pathogenic bacteria by ClpP and the proteasome. *Curr. Opin. Struct. Biol.* **67**, 120–126 (2021).
22. S. H. Becker *et al.*, The Mycobacterium tuberculosis Pup-proteasome system regulates nitrate metabolism through an essential protein quality control pathway. *Proc. Natl. Acad. Sci. U.S.A.* **116**, 3202–3210 (2019).
23. Y. Elharar *et al.*, Survival of mycobacteria depends on proteasome-mediated amino acid recycling under nutrient limitation. *EMBO J.* **33**, 1802–1814 (2014).
24. M. F. Block, C. L. Delley, L. M. Keller, T. T. Stuehlinger, E. Weber-Ban, Electrostatic interactions guide substrate recognition of the prokaryotic ubiquitin-like protein ligase PafA. *Nat. Commun.* **14**, 5266 (2023).
25. J. Laederach, H. Cui, E. Weber-Ban, Pupylated proteins are subject to broad proteasomal degradation specificity and differential depupylation. *PLoS One* **14**, e0215439 (2019).
26. N. Hecht, M. Becher, M. Korman, M. Vishkautzan, E. Gur, Inter- and intramolecular regulation of protein depupylation in Mycobacterium smegmatis. *FEBS J.* **287**, 4389–4400 (2020).
27. D. Ozcelik *et al.*, Structures of Pup ligase PafA and depupylase Dop from the prokaryotic ubiquitin-like modification pathway. *Nat. Commun.* **3**, 1014 (2012).
28. J. H. Yoo, S. C. Kahne, K. H. Darwin, A conserved loop sequence of the proteasome system depupylase Dop regulates substrate selectivity in Mycobacterium tuberculosis. *J. Biol. Chem.* **298**, 102478 (2022).
29. B. K. Strauss, The biosynthesis of coenzyme A in bacteria. *Vitam. Horm.* **61**, 157–171 (2001).
30. M. Yun *et al.*, Structural basis for the feedback regulation of Escherichia coli pantothenate kinase by coenzyme A. *J. Biol. Chem.* **275**, 28093–28099 (2000).
31. R. A. Ivey *et al.*, The structure of the pantothenate kinase· ADP· pantothenate ternary complex reveals the relationship between the binding sites for substrate, allosteric regulator, and antimetabolites. *J. Biol. Chem.* **279**, 35622–35629 (2004).
32. B. S. Hong *et al.*, Prokaryotic type II and type III pantothenate kinases: The same monomer fold creates dimers with distinct catalytic properties. *Structure* **14**, 1251–1261 (2006).
33. R. Yocum, T. Patterson, *Microorganisms and Assays for the Identification of Antibiotics*, U. S. P. a. T. Office, Ed. (OmniGene Bioroducts. Inc., USA, 2004), p. 95.

34. C. Paige, S. D. Reid, P. C. Hanna, A. Claiborne, The type III pantothenate kinase encoded by coaX is essential for growth of Bacillus anthracis. *J. Bacteriol.* **190**, 6271–6275 (2008).
35. N. I. Nicely *et al.*, Structure of the type III pantothenate kinase from Bacillus anthracis at 2.0 angstrom resolution: Implications for coenzyme A-dependent redox biology. *Biochemistry-Us* **46**, 3234–3245 (2007).
36. D. Awasthy *et al.*, Essentiality and functional analysis of type I and type III pantothenate kinases of Mycobacterium tuberculosis. *Microbiology (Reading)* **156**, 2691–2701 (2010).
37. S. T. Cole *et al.*, Massive gene decay in the leprosy bacillus. *Nature* **409**, 1007–1011 (2001).
38. K. Yang, E. Strauss, C. Huerta, H. Zhang, Structural basis for substrate binding and the catalytic mechanism of type III pantothenate kinase. *Biochemistry-Us* **47**, 1369–1380 (2008).
39. K. Yang *et al.*, Crystal structure of a type III pantothenate kinase: Insight into the mechanism of an essential coenzyme A biosynthetic enzyme universally distributed in bacteria. *J. Bacteriol.* **188**, 5532–5540 (2006).
40. N. I. Nicely *et al.*, Structure of the type III pantothenate kinase from Bacillus anthracis at 2.0 A resolution: Implications for coenzyme A-dependent redox biology. *Biochemistry-Us* **46**, 3234–3245 (2007).
41. E. Krissinel, K. Henrick, Inference of macromolecular assemblies from crystalline state. *J. Mol. Biol.* **372**, 774–797 (2007).
42. H. Cui *et al.*, Structures of prokaryotic ubiquitin-like protein Pup in complex with depupylase Dop reveal the mechanism of catalytic phosphate formation. *Nat. Commun.* **12**, 6635 (2021).
43. J. Yao, C. Subramanian, C. O. Rock, S. Jackowski, Human pantothenate kinase 4 is a pseudo-pantothenate kinase. *Protein Sci.* **28**, 1031–1047 (2019).
44. M. J. Pepi *et al.*, A d-phenylalanine-benzoxazole derivative reveals the role of the essential enzyme Rv3603c in the pantothenate biosynthetic pathway of Mycobacterium tuberculosis. *ACS Infect. Dis.* **8**, 330–342 (2022).
45. J. Barandun *et al.*, Prokaryotic ubiquitin-like protein remains intrinsically disordered when covalently attached to proteasomal target proteins. *BMC Struct. Biol.* **17**, 1 (2017).
46. B. N. Chaudhuri *et al.*, The crystal structure of the first enzyme in the pantothenate biosynthetic pathway, ketopantoate hydroxymethyltransferase, from M tuberculosis. *Structure* **11**, 753–764 (2003).
47. M. Bolten *et al.*, Depupylase dop requires inorganic phosphate in the active site for catalysis. *J. Biol. Chem.* **292**, 4044–4053 (2017).
48. V. K. Sambandamurthy *et al.*, A pantothenate auxotroph of Mycobacterium tuberculosis is highly attenuated and protects mice against tuberculosis. *Nat. Med.* **8**, 1171–1174 (2002).
49. J. Stolz, N. Sauer, The fenpropimorph resistance gene FEN2 from Saccharomyces cerevisiae encodes a plasma membrane H+-pantothenate symporter *J. Biol. Chem.* **274**, 18747–18752 (1999).
50. K. J. Saliba, K. Kirk, H+-coupled pantothenate transport in the intracellular malaria parasite *J. Biol. Chem.* **276**, 18115–18121 (2001).
51. D. S. Vallari, C. Rock, Pantothenate transport in Escherichia coli. *J. Bacteriol.* **162**, 1156–1161 (1985).
52. M. Zhang *et al.*, Structure of a pantothenate transporter and implications for ECF module sharing and energy coupling of group II ECF transporters. *Proc. Natl. Acad. Sci. U.S.A.* **111**, 18560–18565 (2014).
53. P. D. Prasad, S. Ramamoorthy, F. Leibach, V. Ganapathy, Characterization of a sodium-dependent vitamin transporter mediating the uptake of pantothenate, biotin and lipoate in human placental choriocarcinoma cells. *Placenta* **18**, 527–533 (1997).
54. J. C. Evans *et al.*, Validation of CoaBC as a bactericidal target in the Coenzyme A pathway of Mycobacterium tuberculosis. *ACS Infect. Dis.* **2**, 958–968 (2016).
55. M. I. Samanovic *et al.*, Proteasomal control of cytokinin synthesis protects Mycobacterium tuberculosis against nitric oxide. *Mol. Cell* **57**, 984–994 (2015).
56. Y. Jo, R. A. DeBose-Boyd, Post-translational regulation of HMG CoA reductase. *Cold Spr. Harbor Perspect. Biol.* **14**, a041253 (2022).
57. K. H. Darwin, Prokaryotic ubiquitin-like protein (Pup), proteasomes and pathogenesis. *Nat. Rev. Microbiol.* **7**, 485–491 (2009).
58. A. Kuberl, T. Polen, M. Bott, The pupylation machinery is involved in iron homeostasis by targeting the iron storage protein ferritin. *Proc. Natl. Acad. Sci. U.S.A.* **113**, 4806–4811 (2016).
59. M. Merkamm, C. Chassagnole, N. D. Lindley, A. Guyonvarch, Ketopantoate reductase activity is only encoded by ilvC in Corynebacterium glutamicum. *J. biotechnol.* **104**, 253–260 (2003).
60. A. Küberl *et al.*, Pupylated proteins in Corynebacterium glutamicum revealed by MudPIT analysis. *Proteomics* **14**, 1531–1542 (2014).
61. A. Punjani, J. L. Rubinstein, D. J. Fleet, M. A. Brubaker, cryoSPARC: algorithms for rapid unsupervised cryo-EM structure determination. *Nat. Methods* **14**, 290–296 (2017).
62. T. Bepler, K. Kelley, A. J. Noble, B. Berger, Topaz-Denoise: general deep denoising models for cryoEM and cryoET. *Nat. Commun.* **11**, 5208 (2020).
63. A. Punjani, H. Zhang, D. J. Fleet, Non-uniform refinement: adaptive regularization improves single-particle cryo-EM reconstruction. *Nat. Methods* **17**, 1214–1221 (2020).
64. J. Jumper *et al.*, Highly accurate protein structure prediction with AlphaFold. *Nature* **596**, 583–589 (2021).
65. M. Mirdita *et al.*, ColabFold: making protein folding accessible to all. *Nat. Methods* **19**, 679–682 (2022).
66. D. Liebschner *et al.*, Macromolecular structure determination using X-rays, neutrons and electrons: Recent developments in Phenix. *Acta Crystallogr. D Struct. Biol.* **75**, 861–877 (2019).
67. E. F. Pettersen *et al.*, UCSF ChimeraX: Structure visualization for researchers, educators, and developers. **30**, 70–82 (2021).
68. D. Liebschner *et al.*, Macromolecular structure determination using X-rays, neutrons and electrons: recent developments in Phenix. *Acta Crystallogr. D Struct. Biol.* **75**, 861–877 (2019).
69. P. Emsley, B. Lohkamp, W. G. Scott, K. Cowtan, Features and development of Coot. *Acta Crystallogr. D Biol. Crystallogr.* **66**, 486–501 (2010).
70. C. J. Williams *et al.*, MolProbity: More and better reference data for improved all-atom structure validation. *Protein Sci.* **27**, 293–315 (2018).
71. B. A. Barad *et al.*, EMRinger: side chain-directed model and map validation for 3D cryo-electron microscopy. *Nat. Methods* **12**, 943–946 (2015).
72. Y. Z. Tan *et al.*, Addressing preferred specimen orientation in single-particle cryo-EM through tilting. *Nat. Methods* **14**, 793–796 (2017).
73. A. A. Schaffer *et al.*, Improving the accuracy of PSI-BLAST protein database searches with composition-based statistics and other refinements. *Nucleic Acids Res.* **29**, 2994–3005 (2001).
74. S. Deorowicz, A. Debudaj-Grabysz, A. Gudys, FAMSA: Fast and accurate multiple sequence alignment of huge protein families. *Sci. Rep.* **6**, Article ID 33964, (2016).
75. R. A. Festa *et al.*, A novel copper-responsive regulon in Mycobacterium tuberculosis. *Mol. Microbiol.* **79**, 133–148 (2011).
76. G. Limon, N. M. Samhadaneh, A. Pironti, K. H. Darwin, Aldehyde accumulation in Mycobacterium tuberculosis with defective proteasomal degradation results in copper sensitivity. *mBio* **14**, e0036323 (2023).
77. B. Langmead, S. L. Salzberg, Fast gapped-read alignment with Bowtie 2. *Nat. Methods* **9**, 357–359 (2012).
78. H. Li *et al.*, The sequence alignment/map format and SAMtools. *Bioinformatics* **25**, 2078–2079 (2009).
79. Y. Liao, G. K. Smyth, W. Shi, featureCounts: An efficient general purpose program for assigning sequence reads to genomic features. *Bioinformatics* **30**, 923–930 (2014).
80. M. I. Love, W. Huber, S. Anders, Moderated estimation of fold change and dispersion for RNA-seq data with DESeq2. *Genome. Biol.* **15**, 550 (2014).
81. R. C. Team, *R: A Language and Environment for Statistical Computing* (R Foundation for Statistical Computing, Vienna, Austria, 2021).
82. H. Wickham *et al.*, Welcome to the Tidyverse. *J. Open Sour. Softw.* **4**, 1686 (2019).
83. S. C. Kahne, K. H. Darwin, A. Pironti, Identification of a depupylation regulator for an essential enzyme in *Mycobacterium tuberculosis*. NCBI Gene Expression Omnibus. https://www.ncbi.nlm.nih.gov/geo/query/acc.cgi?acc=GSE260838. Deposited 4 March 2024.